PAPER

Energy correction based on fluorescence attenuation of DAMPE

View the article online for updates and enhancements.

Energy correction based on fluorescence attenuation of DAMPE

Li-Bo Wu, Yun-Long Zhang, Zhi-Yong Zhang, Yi-Feng Wei, Si-Cheng Wen, Hao-Ting Dai, Cheng-Ming Liu, Xiao-Lian Wang, Zi-Zong Xu and Guang-Shun Huang

State Key Laboratory of Particle Detection and Electronics, University of Science and Technology of China, Hefei 230026, China; *zhzhy@ustc.edu.cn, weiyf@ustc.edu.cn*
Department of Modern Physics, University of Science and Technology of China, Hefei 230026, China

Abstract The major scientific goals of the DArk Matter Particle Explorer (DAMPE) are to study cosmic-ray electrons (including positrons) and gamma rays from 5 GeV to 10 TeV and nuclei from Z = 1 to 26 up to 100 TeV. The deposited energy measured by the Bismuth Germanate Oxide (BGO) calorimeter of DAMPE is affected by fluorescence attenuation in BGO crystals that are 600 mm long. In this work, an in-orbit attenuation calibration method is reported, and energy correction of the sensitive detector unit of the BGO calorimeter is also presented.

Key words: DAMPE — BGO calorimeter — fluorescence attenuation — dark matter

1 INTRODUCTION

The DArk Matter Particle Explorer (DAMPE) (Chang et al. 2017; DAMPE Collaboration et al. 2017; Ambrosi et al. 2019; Yuan & Feng 2018), which is a satellite-borne experiment funded by the Chinese Academy of Sciences, was launched into a sun-synchronous orbit at an altitude of 500 km in December 2015 from the Jiuquan Satellite Launch Center. The scientific objectives of DAMPE include searching for the signature of dark matter particles (Bertone et al. 2005; Lu et al. 2014), understanding the mechanisms of particle acceleration operating in astrophysical sources (An et al. 2019), and studying gamma-ray emission from Galactic and extragalactic sources (Duan et al. 2019; Xu et al. 2018).

DAMPE, as shown in Figure 1, consists of four sub-detectors. From top to bottom, they are the Plastic Scintillator Detector (PSD) (Ding et al. 2019; Ma et al. 2019), Silicon-Tungsten tracKer (STK) (Azzarello et al. 2016), Bismuth Germanium Oxide (BGO) calorimeter (Wu et al. 2018; Zhang et al. 2015, 2019), and NeUtron Detector (NUD) (He et al. 2016). The PSD, which is composed of two orthogonal layers of plastic scintillator strips with dimensions of $884 \times 28 \times 10$ mm, is designed to measure the charge of incoming nuclei via the Z^2 dependence of the specific ionization loss in a double layer up to Z = 26, and it aids in the discrimination between charged particles and photons. The STK is composed of six or-

thogonal layers of position-sensitive silicon microstrip detectors. Three layers of tungsten are inserted inside layers 2, 3, and 4 to convert gamma rays in electron-positron pairs. The STK enables reconstruction of the trajectory and charge of an event. The BGO calorimeter contains 14 layers with 31 radiation lengths and ∼1.6 nuclear interaction lengths in total (Wei et al. 2016). Each layer has 22 BGO bars, which are arranged horizontally. The BGO bars of neighboring layers are arranged in an orthogonal way to measure the energy deposition and profile of hadron and electromagnetic showers developed in the BGO calorimeter. Moreover, the BGO provides the trigger for the whole DAMPE system. The NUD is composed of four boron-loaded plastic scintillators, each with a set of photomultiplier tubes (PMTs) and related electronics. It provides additional electron-hadron discrimination, which is important for energies above TeV.

Because of the thick BGO calorimeter (Wu et al. 2018), the energy range of DAMPE can cover from 5 GeV to 10 TeV for electrons and gamma rays and from tens of GeV to hundreds of TeV for cosmic protons and heavier nuclei. The BGO calorimeter is composed of 308 BGO crystal bars with dimensions $25 \times 25 \times 600$ mm (produced by the Shanghai Institute of Ceramics), which is the longest BGO crystal available at the time of development. The deposited energy in a BGO bar is independently measured by means of the fluorescent quantities collected by the PMTs at the two ends. The fluorescent photons trans-
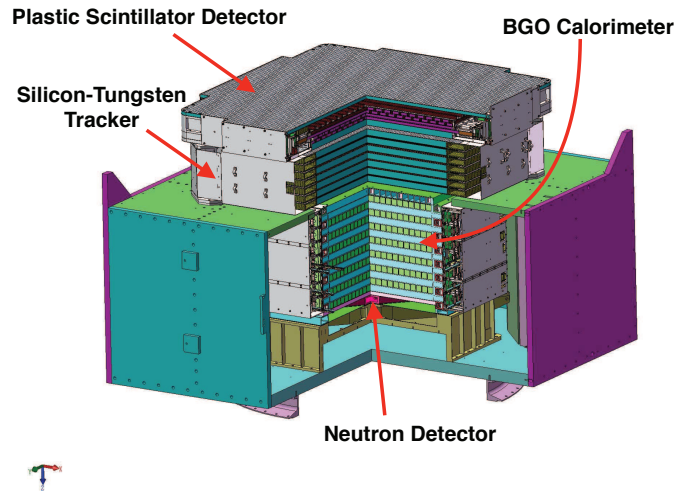
Fig. 1 Side view of the DAMPE detector.

Fig. 2 BGO crystal with dimension of $25 \times 25 \times 600\,\text{mm}$.
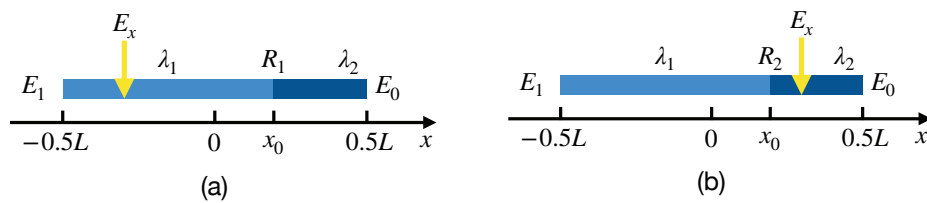

Fig. 3 Schematic plots of a BGO bar with its parameters of interest, showing (a) a hit position on the left side and (b) a hit position on the right side.
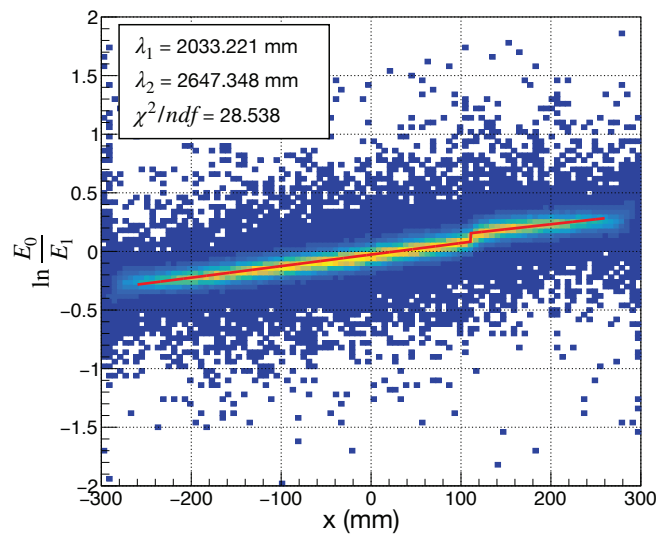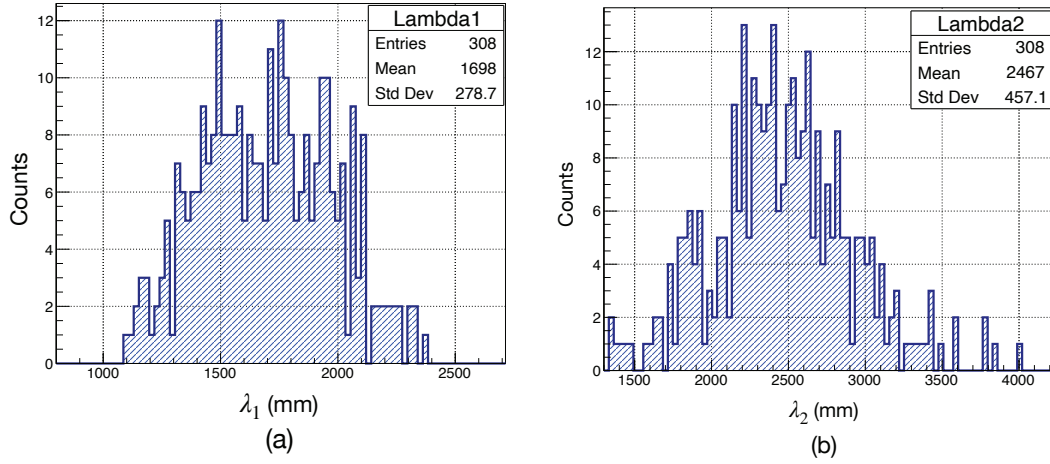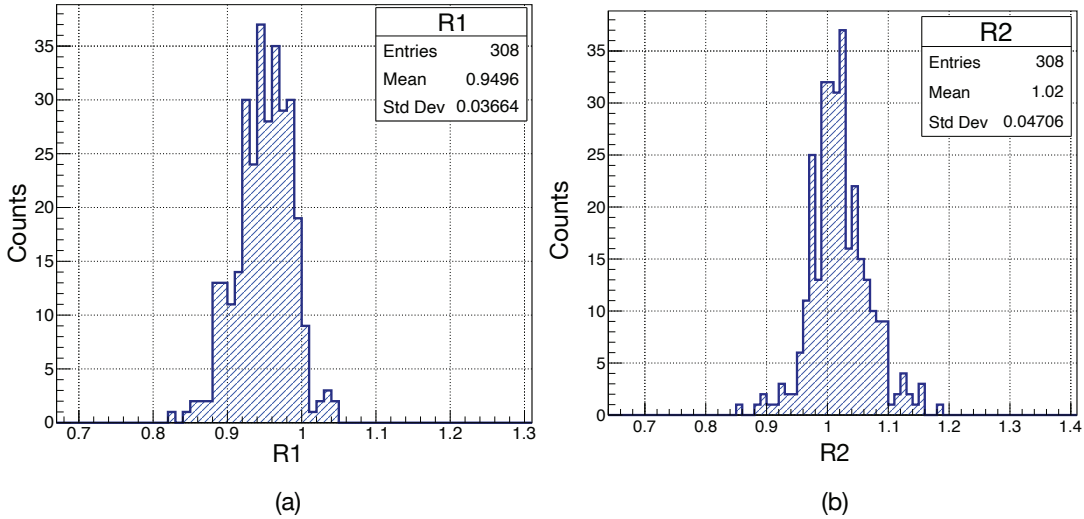

Fig. 4 Scatterplot of $\ln \frac{E_0}{E_1}$ versus hit position x. The fit range is from $-260\,\text{mm}$ to $260\,\text{mm}$.

Fig. 5 Distributions of attenuation lengths of all BGO crystals: (a) λ_1; (b)λ_2.

Fig. 6 Distribution ratios of the variation of scintillation intensity: (a) R_1; (b) R_2.

mitted along the BGO bar are unavoidably attenuated, so energy correction for this fluorescent attenuation must be taken into account.

2 ATTENUATION LENGTH CALIBRATION

Figure 2 shows a 600-mm-long BGO crystal bar (Ji et al. 2014). PMTs are connected to the BGO crystal at both ends (Side0 and Side1) (Zhang et al. 2015, 2012; Feng et al. 2015) to collected fluorescent lights, which is exponentially attenuated with the distance between the hit position and the PMT. Limited by crystal growth technology at the time of development, there has to be a black shadow called a cutoff point marked by a red cycle in Figure 2; When scintillating light pass through this region, the absorption and reflection efficiency of the spot to them is very different from other regions. This will cause the energy ratio of reconstruction at both ends to jump here, as shown in

Figure 4. In order to eliminate this effect, this paper developed a method to calibrate the attenuation lengths of the crystal at both sides of the spot respectively, and apply them to energy correction.

2.1 Method of Calibration

By considering the energy resolution and the flux of incident particles, all cosmic-ray events are used to calibrate the scintillation attenuation length. The following event selection criteria should be applied:

– Energy requirement: The total energy deposited in the BGO calorimeter should be $> 10\,\mathrm{GeV}$.
– Track requirement: The BGO track should match the STK track to get an accurate position measurement of the track.

- BarID match requirement: The BGO crystal hit by the track of each layer must have maximum energy deposition in the layer.
- Acceptance requirement: The events should be in the range of the acceptance angle of the DAMPE detector.

Figure 3 illustrates the true deposited energy E_x at hit position x, energies E_0, E_1 measured from the side 0 and side 1, independently, and the cutoff point x_0. The origin of the x axis is set at the middle of the BGO bar of total length $L = 600$ mm. λ_1 and λ_2 are the fluorescent attenuation lengths of the two parts ($-0.5L$ to x_0) and (x_0 to $0.5L$), respectively. There are two cases: Either the hit position is to the left (Fig. 3(a)) of the cutoff point or it is to the right (Fig. 3(b)); the calibration methods are similar. For the case of Figure 3(a), following the law of fluorescent attenuation, the measured energies E_0 and E_1, which are proportional to the fluorescent quantities collected by the PMTs of side 0 and 1, can be expressed as:

$$E_0 = E_x \times e^{-\frac{(x_0-x)}{\lambda_1}} \times e^{-\frac{(0.5L-x_0)}{\lambda_2}} \times R_1, \quad (1)$$

$$E_1 = E_x \times e^{-\frac{x+0.5L}{\lambda_1}}, \quad (2)$$

where E_x is the true deposited energy at position x (from -300 to 300 mm) in the BGO bar and R_1 in Equation (1) is the transparent coefficient when fluorescent photons pass through the cut point x_0 from the left to right.

The attenuation length of the left part ($x < x_0$) can be calibrated with the following function derived from Equations (1) and (2):

$$\ln\left(\frac{E_0}{E_1}\right) = \frac{2x}{\lambda_1} \\ + \left[\frac{0.5L-x_0}{\lambda_1} + \frac{x_0-0.5L}{\lambda_2} + \ln R_1\right]. \quad (3)$$

Similarly, for the cases when particles are incident on the right ($x > x_0$), the attenuation length λ_2 can be calibrated by using Equation (4), where R_2 is the transparent coefficient when fluorescent photons pass through the cutoff point x_0 from right to left.

$$\ln\left(\frac{E_0}{E_1}\right) = \frac{2x}{\lambda_2} \\ + \left[\frac{0.5L+x_0}{\lambda_1} - \frac{0.5L+x_0}{\lambda_2} + \ln \frac{1}{R_2}\right]. \quad (4)$$

Taking an example of the attenuation length calibration of a BGO bar (No. 10, layer 3), the hit position x and the measured energies E_0 and E_1 are, event by event, reconstructed according the event track fitting and ADC counts readout from electronics of the both sides. Figure 4 shows a typical scatterplot of $\ln \frac{E_0}{E_1}$ versus x of the BGO bar at No. 10 of layer 3.

2.2 Calibration Results

Fitting the scatterplot of Figure 4 with the Equations (3) and (4) gives fluorescent attenuation lengths of the BGO bar of $\lambda_1 = 2033$ mm and $\lambda_2 = 2647$ mm. The parameters R_1 and R_2 can be calculated from the intercept of the fitting line. The same calibration program was applied to all 308 piecse of the BGO bars. Figures 5 and 6 show the distributions of λ_1 and λ_2 and R_1 and R_2, respectively, for the BGO calorimeter.

A database of the calibration parameters of the 308 pieces of the BGO bar (λ_1, λ_2 and R_1, R_2, x_0) has been set up for the program of the following energy correction.

3 ENERGY CORRECTION BASED ON ATTENUATION LENGTH

In the experiment, the measured energies E_0 and E_1 are different from the true deposited energy at the hit position x because of the fluorescent attenuation, as shown in Equations (1) and (2). Therefore, it is necessary to perform an energy correction to account for fluorescence attenuation for each BGO crystal.

3.1 Method of Energy Correction

By using the database, the true deposited energy at hit position x can be, event by event, corrected for each BGO bar by means of the following formulas:

$$E_{x_0} = E_0 \times e^{\frac{x_0-x}{\lambda_1}} e^{\frac{0.5L-x_0}{\lambda_2}} \times \frac{1}{R_1}, \quad (5)$$

$$E_{x_1} = E_1 \times e^{\frac{x+0.5L}{\lambda_1}}, \quad (6)$$

$$E_{x_0} = E_0 \times e^{\frac{0.5L-x}{\lambda_2}}, \quad (7)$$

$$E_{x_1} = E_1 \times e^{\frac{x-x_0}{\lambda_2}} \times e^{\frac{x_0+0.5L}{\lambda_1}} \times \frac{1}{R_2}, \quad (8)$$

where Equations (5) and (6) are energy correction for cases when particles hit the left part ($x < x_0$) of the BGO crystal, while Equations (7) and (8) are for cases when particles hit the right part ($x \geq x_0$). E_{x_0} and E_{x_1} are the energies at side 0 and side 1 after the attenuation correction, respectively. Moreover, the hit position reconstructed by track of each layer is used to correct the energy of each BGO bars of the corresponding layer.

The total deposited energy can be obtained by using the correction method on all BGO crystals, and the distributions of the ratio of total deposited energy at the two sides before and after correction are shown in Figures 9(a) and 9(b), respectively. The peak value is 0.998 after correction, which is more closer to 1 than the result before correction, and the standard deviation after correction is 0.046, which is much less than the result of 0.141 before correction.
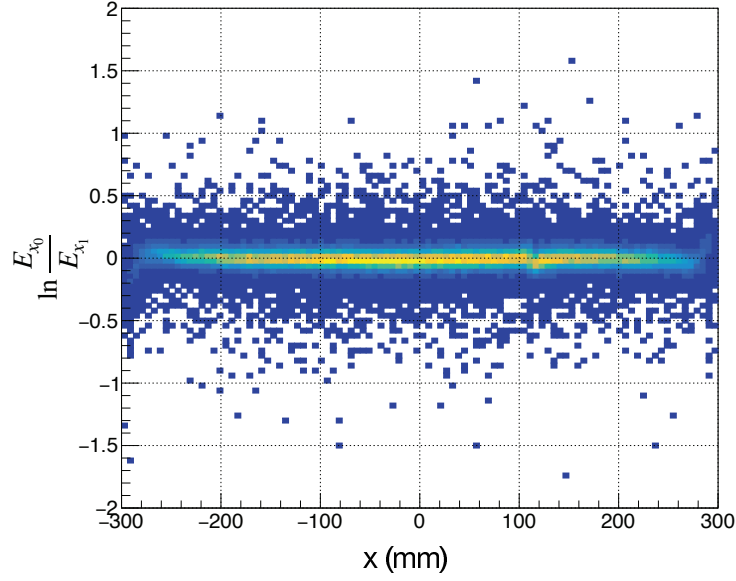
Fig. 7 Scatterplot of $\ln \frac{E_{x_0}}{E_{x_1}}$ versus hit position x after energy correction.

(a)

(b)
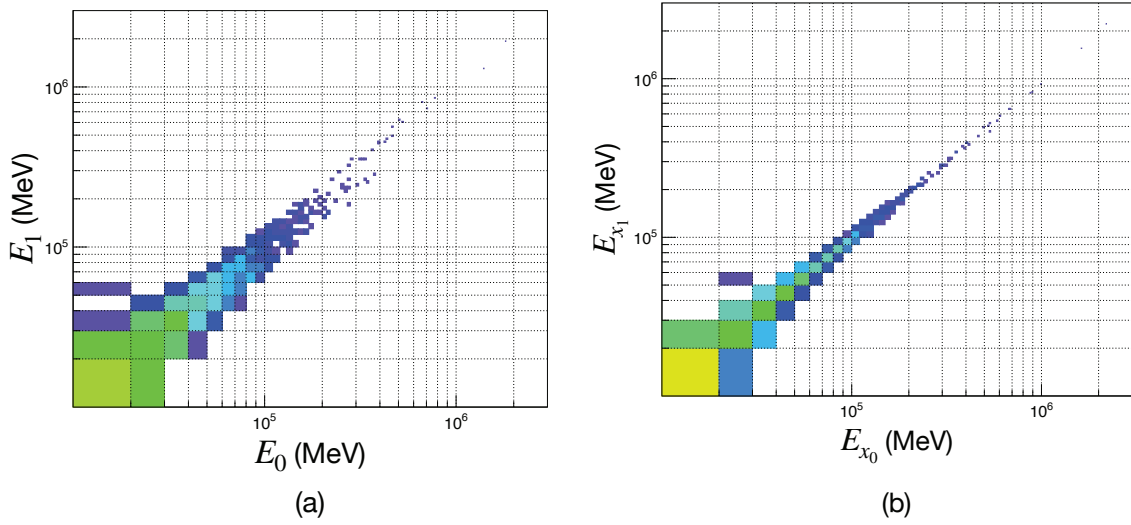
Fig. 8 Comparison of the relationships of the energies at the two sides (a) before correction and (b) after correction.

3.2 Energy Correction Results

The correlation between $\ln \frac{E_0}{E_1}$ and hit position (x) of the BGO bar (No. 10, layer 3) after correction is shown in Figure 7. Note that the distribution is flatter than that in Figure 4, without a jump at x_0. Figure 8 shows a comparison of the relationship of the energies at the two sides before (Fig. 8(a)) and after (Fig. 8(b)) correction. The plot in Figure 8(b) demonstrates that, after energy correction, E_{x_0} and E_{x_1} measured at the two sides are getting closer to each other and become two independent measures of the true deposited energy at hit position x. Therefore, the

correction program will increase the energy measurement accuracy and redundancy.

4 CONCLUSIONS

There really is a fluorescence attenuation in BGO crystal, which will influence the energy reconstructed at both sides. An in-orbit method to calibrate attenuation length based on the unique BGO crystals of DAMPE has been studied, and a database of calibration parameters has been set up. Upon completion of the energy correction for fluorescence attenuation, the consistency between energy measurements at the two sides was raised from 0.941 to 0.998, E_{x_0} and E_{x_1} became two independent measurements of the true deposit-
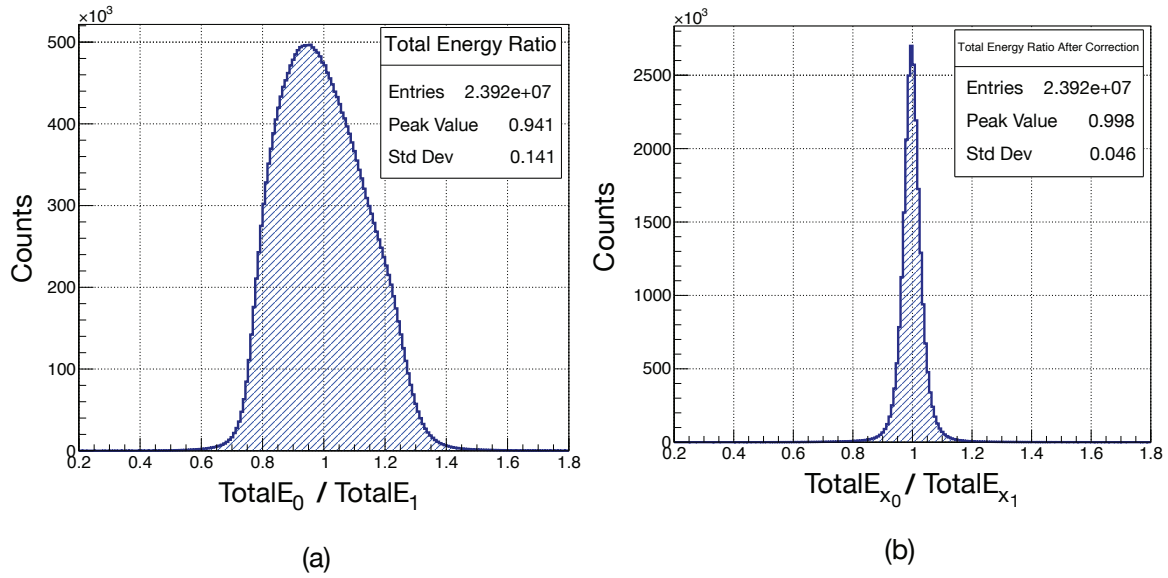
Fig. 9 Ratios of the total deposited energies reconstructed from side 0 and side 1 of all BGO crystals: (a) before correction; (b) after correction.

ed energy E_x, and the energy resolution and redundancy capability of the BGO calorimeter were significantly improved.

References

Ambrosi, G., An, Q., Asfandiyarov, R., et al. 2019, Astroparticle Physics, 106, 18

An, Q., Asfandiyarov, R., Azzarello, P., et al. 2019, Science Advances, 5, eaax3793

Azzarello, P., Ambrosi, G., Asfandiyarov, R., et al. 2016, Nuclear Instruments and Methods in Physics Research A, 831, 378

Bertone, G., Hooper, D., & Silk, J. 2005, Phys. Rep., 405, 279

Chang, J., Ambrosi, G., An, Q., et al. 2017, Astroparticle Physics, 95, 6

DAMPE Collaboration, Ambrosi, G., An, Q., et al. 2017, Nature, 552, 63

Ding, M., Zhang, Y.-P., Zhang, Y.-J., et al. 2019, RAA (Research in Astronomy and Astrophysics), 19, 047

Duan, K.-K., Jiang, W., Liang, Y.-F., et al. 2019, RAA (Research in Astronomy and Astrophysics), 19, 132

Feng, C., Zhang, D., Zhang, J., et al. 2015, IEEE Transactions on Nuclear Science, 62, 3117

He, M., Ma, T., Chang, J., et al. 2016, Chinese Astronomy and Astrophysics, 40, 474

Ji, Z., Ni, H., Yuan, L., Chen, J., & Wang, S. 2014, Nuclear Instruments and Methods in Physics Research A, 753, 143

Lu, T.-S., Dong, T.-K., & Wu, J. 2014, RAA (Research in Astronomy and Astrophysics), 14, 520

Ma, P.-X., Zhang, Y.-J., Zhang, Y.-P., et al. 2019, RAA (Research in Astronomy and Astrophysics), 19, 082

Wei, Y., Zhang, Z., Zhang, Y., et al. 2016, IEEE Transactions on Nuclear Science, 63, 548

Wu, L., Wen, S., Liu, C., et al. 2018, IEEE Transactions on Nuclear Science, 65, 2007

Xu, Z.-L., Duan, K.-K., Shen, Z.-Q., et al. 2018, RAA (Research in Astronomy and Astrophysics), 18, 027

Yuan, Q., & Feng, L. 2018, Science China Physics, Mechanics, and Astronomy, 61, 101002

Zhang, Y.-L., Li, B., Feng, C.-Q., et al. 2012, Chinese Physics C, 36, 71

Zhang, Y.-Q., Guo, J.-H., Liu, Y., et al. 2019, RAA (Research in Astronomy and Astrophysics), 19, 123

Zhang, Z., Zhang, Y., Dong, J., et al. 2015, Nuclear Instruments and Methods in Physics Research A, 780, 21